

# The a-axis optical conductivity of detwinned ortho-II $\text{YBa}_2\text{Cu}_3\text{O}_{6.50}$

J. Hwang<sup>1</sup>, J. Yang<sup>1</sup>, T. Timusk<sup>1</sup>, S.G. Sharapov<sup>1</sup>, J.P. Carbotte<sup>1</sup>, D.A. Bonn<sup>2</sup>, Ruixing Liang<sup>2</sup>, and W.N. Hardy<sup>2\*</sup>

<sup>1</sup>*Department of Physics and Astronomy, McMaster University, Hamilton, ON L8S 4M1, Canada*

<sup>2</sup>*Department of Physics and Astronomy, University of British Columbia, Vancouver, BC V6T 1Z1, Canada*

(Dated: November 21, 2018)

The a-axis optical properties of a detwinned single crystal of  $\text{YBa}_2\text{Cu}_3\text{O}_{6.50}$  in the ortho II phase (Ortho II Y123,  $T_c = 59$  K) were determined from reflectance data over a wide frequency range (70 - 42 000  $\text{cm}^{-1}$ ) for nine temperature values between 28 and 295 K. Above 200 K the spectra are dominated by a broad background of scattering that extends to 1 eV. Below 200 K a shoulder in the reflectance appears and signals the onset of scattering at 400  $\text{cm}^{-1}$ . In this temperature range we also observe a peak in the optical conductivity at 177  $\text{cm}^{-1}$ . Below 59 K, the superconducting transition temperature, the spectra change dramatically with the appearance of the superconducting condensate. Its spectral weight is consistent, to within experimental error, with the Ferrell-Glover-Tinkham (FGT) sum rule. We also compare our data with magnetic neutron scattering on samples from the same source that show a strong resonance at 31 meV. We find that the scattering rates can be modeled as the combined effect of the neutron resonance and a bosonic background in the presence of a density of states with a pseudogap. The model shows that the decreasing amplitude of the neutron resonance with temperature is compensated for by an increasing of the bosonic background yielding a net temperature independent scattering rate at high frequencies. This is in agreement with the experiments.

PACS numbers: 74.25.Gz, 74.62.Dh, 74.72.Hs

The complete phase diagram of the high temperature superconducting (HTSC) cuprates is still under intense debate. The normal state, particularly in the underdoped region, is dominated by a variety of not-well-understood cross-over phenomena that may either be precursors to superconductivity or competing states. These include the pseudogap [1], the magnetic resonance [2, 3, 4], the anomalous Nernst effect [5, 6], stripe order [7, 8, 9, 10] and possible superconducting fluctuations [11, 12]. The situation is further complicated by the presence of disorder and the practical considerations that lead to a situation where a given cuprate is not investigated with all the available experimental techniques. Ideally, one would like to have a system where disorder is minimized and several experimental techniques can be used with the same crystals. As a step in that direction we present detailed a-axis optical data on the highly ordered ortho-II phase of  $\text{YBa}_2\text{Cu}_3\text{O}_{6.50}$  (Ortho II Y123) and compare these data with recent results from magnetic neutron scattering and microwave spectroscopy on crystals from the same source.

An important motivation for a comparison between transport properties and the magnetic neutron resonance comes from the observation that the carrier life time, as measured by infrared spectroscopy, is dominated by a bosonic mode [13, 14, 15, 16, 17] whose frequency and intensity, as a function of temperature and doping level, tracks the inelastic magnetic resonance at 41 meV with in-plane momentum transfer of  $(\pi, \pi)$  [15, 16]. The magnetic resonance has also been invoked to explain other self-energy effects such as the kink in the dispersion of angle-resolved photo emission spectra (ARPES) [18, 19, 20, 21] and as a hump-peak struc-

ture in tunneling spectra [22]. These effects have also been attributed to the electron-phonon interaction [23]. While the bosonic excitation may not be the fundamental engine of superconductivity [16, 24], nevertheless it is important to map out the regions in the phase diagram where it can be found and correlate the various experiments that yield evidence of its presence.

The  $\text{YBa}_2\text{Cu}_3\text{O}_{7-x}$  (Y123) material has been one of the most thoroughly studied of all the HTSC systems but, like most cuprates, it suffers from disorder associated with the charge reservoir layer, in the case of Y123, disordered oxygen chains. However, at an oxygen doping level of  $x = 0.50$ , an ordered ortho-II phase occurs with alternating full and empty  $\text{CuO}$  chains, doubling the unit cell along the a-direction, and yielding a well ordered stoichiometric compound [25, 26]. A further advantage of this system is the availability of very large crystals, suitable for neutron scattering. A disadvantage of the Y123 system is that the crystals are not easily vacuum-cleaved and as a result, surface sensitive probes such as angle resolved photoemission or scanning tunneling microscopy have been used less with Y123. In contrast  $\text{Bi}_2\text{Sr}_2\text{CaCu}_2\text{O}_8$  (Bi-2212) cleaves easily and unlike Y123, can also be overdoped. Optical spectroscopy has the advantage of working on both systems equally well and offers a bridge between the ARPES surface sensitive experiments and the large-volume probe of neutron scattering.

The paper is organized as follows. We start with a brief introduction to the experimental method followed by a presentation of the raw reflectance data and an analysis where we use the extended Drude model to extract the various optical constants, in particular the real and

imaginary parts of the scattering rate. To improve the accuracy of the data, we first remove known features in the conductivity spectra such as the transverse optical phonons and the delta-function response of the superconducting condensate. The measured scattering rates are then compared with a theoretical model. We next discuss the overall results by comparing them with data from other experiments on Ortho II Y123, in particular recent neutron data[27] on samples from the same source.

## EXPERIMENTAL METHOD AND RESULTS.

The detwinned ortho-II  $\text{YBa}_2\text{Cu}_3\text{O}_{6.50}$  sample used in this study was grown by a flux method using  $\text{BaZrO}_3$  crucibles [28], annealed under pure oxygen gas flow at  $760^\circ\text{C}$ , and detwinned at  $300^\circ\text{C}$  by applying uni-axial stress of 100 atm along the a-direction [25]. The dimension of the sample is  $1.5 \times 1 \times 0.2 \times \text{mm}^3$ . The nearly normal-incident reflectance of the sample was measured over a wide frequency range ( $70 - 42000 \text{ cm}^{-1}$ ) at nine temperatures between 28 K and 295 K with a Bruker IFS 66v/S Fourier transform spectrometer with linearly polarized light. A polished stainless steel mirror was used as an intermediate reference to correct for instrumental drifts with time and temperature. An *in situ* evaporated gold film on the sample was the absolute reflectance reference [29]. The reflectance of the gold films was in turn calibrated with a polished stainless steel sample where we relied on the Drude theory and the dc resistivity as the ultimate reference. An advantage of this technique is that it corrects for geometrical effects of an irregular surface. The *in situ* gold evaporation technique gives an absolute accuracy of the reflectance of better than  $\pm 0.5\%$ . For the reflectance data above  $14\,000 \text{ cm}^{-1}$  we used aluminum instead of gold as the coating material.

	28 K			100 K			295 K		
	$\omega_{pj}$	$\omega_j$	$\gamma_j$	$\omega_{pj}$	$\omega_j$	$\gamma_j$	$\omega_{pj}$	$\omega_j$	$\gamma_j$
Drude	6000	0	310	11 200	0	490	11 200	0	1500
Extra	8500	0	1	5400	1	1			
Phonons	430	190	3	500	190	4	225	189	7
	470	257	3.5	400	257	3	350	255	10
	720	358	4	690	358	3.5	520	356	13
	549	599	13	555	598	15	430	587	17
S1	950	178	9	470	175	6			
				355	182	4.5			
$\epsilon_\infty = 3.63$									

TABLE I: The fitting parameters of Ortho II Y123 reflectance at three temperatures,  $T = 28 \text{ K}$ ,  $100 \text{ K}$ , and  $295 \text{ K}$ . The unit of  $\omega_{pj}$ ,  $\omega_j$ , and  $\gamma_j$  is  $\text{cm}^{-1}$ . An extra band for  $T = 28 \text{ K}$  is the super fluid band at zero frequency. The extra band for  $T = 100 \text{ K}$  shows additional spectral weight at low frequency at low temperature (see Fig. 5). The peak S1 splits at 100 K into two components.

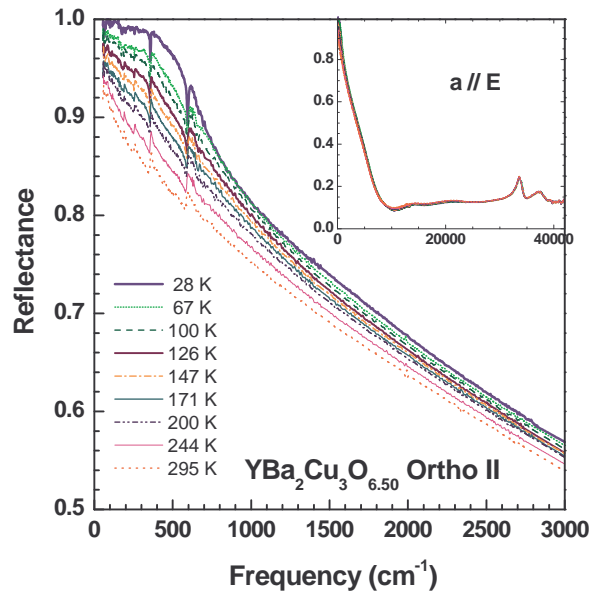


FIG. 1: The a-axis reflectance of Ortho II Y123 at nine temperatures. There is a broad band of absorption giving rise to a region of negative curvature of the reflectance between  $350$  and  $600 \text{ cm}^{-1}$ . At high temperature the curvature is positive at all frequencies. The inset shows the high frequency reflectance.

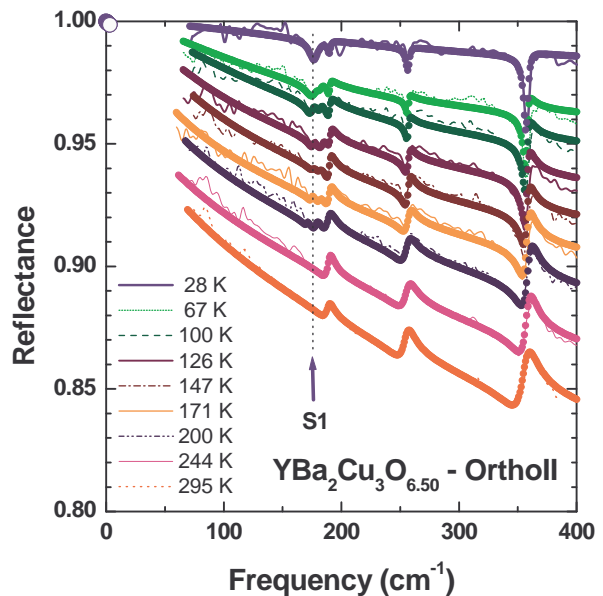


FIG. 2: The low frequency reflectance is shown as thin lines and an oscillator fit is shown as heavy lines. The data are fitted with a Drude band and a series of oscillators, one of which is a strong electronic mode marked S1. In the superconducting state, an oscillator at zero frequency is added to represent the superconducting condensate. The oscillator parameters are shown in Table I. The open circles near zero frequency are reflectance data at 28 K from a microwave measurement [33].

Figure 1 shows the raw reflectance data for nine different temperatures in the frequency region from  $75 \text{ cm}^{-1}$

to  $3000 \text{ cm}^{-1}$ . The inset extends the data up to  $42\,000 \text{ cm}^{-1}$ . A strong temperature dependence is observed in the low frequency range but becomes weaker at higher frequencies. Two specific features show temperature dependent amplitudes: a broad shoulder at  $\approx 400 \text{ cm}^{-1}$  and a less obvious depression in reflectance at  $175 \text{ cm}^{-1}$ . In addition, signatures of well-known transverse optical phonons can be seen as sharp minima in the low temperature spectra [30, 31, 32]. At low temperature the overall curvature of the reflectance is negative at low frequencies changing to a positive curvature at high frequency, which gives rise to an inflection point at  $\approx 700 \text{ cm}^{-1}$ . The inset shows the high frequency reflectance with a prominent plasma edge at  $13\,000 \text{ cm}^{-1}$  and a relatively weak temperature dependence above  $25\,000 \text{ cm}^{-1}$ .

Figure 2 shows the lowest frequency range on an expanded scale. In addition to the transverse phonons, we observe a new feature at  $175 \text{ cm}^{-1}$ , that appears below  $171 \text{ K}$ , and is denoted S1. The thin lines are the measured reflectance curves and the solid thick lines are oscillator fits where the phonons have been modeled as Drude-Lorentz oscillators. The electronic background is represented as a broad Drude peak in the normal state and a two-fluid model with an additional delta function at the origin in the superconducting state. The parameters used in the fit are shown in Table I. From the fit we get a superconducting condensate density of  $72 \times 10^6 \text{ cm}^{-2}$  expressed as the square of a plasma frequency in  $\text{cm}^{-1}$ . This corresponds to a penetration depth of  $1900 \text{ \AA}$ . In comparison, the recent Gd Zero-field Electron Spin Resonance (ESR) measurements on samples from the same source yield a penetration depth of  $2000 \text{ \AA}$  and are shown as open circles at very low frequency at  $28 \text{ K}$  [33]. Our estimated overall error in the absolute value of the reflectance of  $\pm 0.5 \%$  translates to a  $\pm 300 \text{ \AA}$  error in penetration depth. We conclude that our data are in agreement with the ESR results, consistent with errors associated with the measurement of absolute reflectance. If we assume an overall monotonic variation of the fitted curves with temperature, we can estimate, from the deviation from this monotonicity, a relative error of  $0.2 \%$  for the temperature dependence of the reflectance. Finally, from the noise level of the spectra, estimated to be  $0.05 \%$  at  $300 \text{ cm}^{-1}$  and rising to  $0.3 \%$  at  $100 \text{ cm}^{-1}$ , we can set an upper limit of  $250 \text{ cm}^{-1}$  to the plasma frequency of any phonon features we could have missed above  $200 \text{ cm}^{-1}$ . This limit would be higher at lower frequencies.

The optical conductivity and the other optical constants were determined from the measured a-axis reflectance by Kramers-Kronig analysis [34], for which extrapolations to  $\omega \rightarrow 0$  and  $\infty$  must be supplied. For  $\omega \rightarrow 0$ , the reflectance was extrapolated by assuming a Hagen-Rubens frequency dependence in the normal state,  $(1 - R) \propto \omega^{1/2}$ , and below  $T_c$  an  $(1 - R) \propto \omega^4$  extrapolation was used. We used the oscillator fits shown in Fig. 2 to investigate the sources of error arising from the low

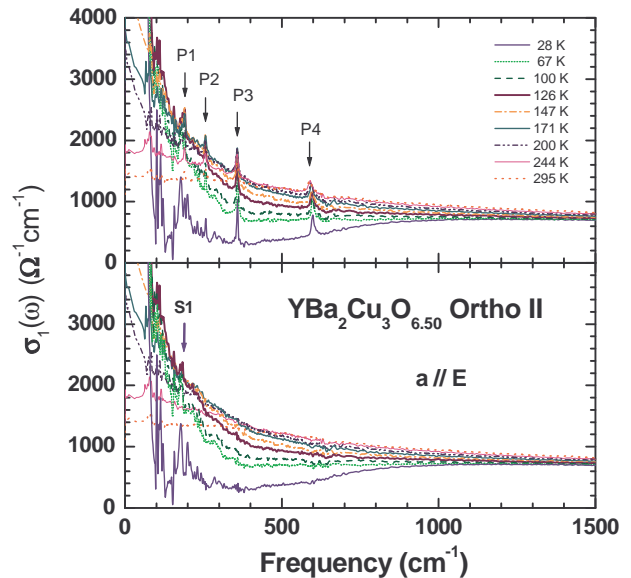


FIG. 3: The upper panel shows the optical conductivity where several prominent phonon peaks have been identified as P1, P2 etc. In the lower panel the phonon peaks (P1 to P4) have been removed. A complex set of absorption bands can be seen at low temperature dominated by a broad peak at  $177 \text{ cm}^{-1}$  designated as S1.

frequency extrapolations. The reflectance was extended to high-frequency (between  $40\,000$  and  $350\,000 \text{ cm}^{-1}$ ) using data from Romberg *et al.* [35]. Free-electron behavior ( $R \propto \omega^{-4}$ ) was assumed to hold at higher frequencies.

The top panel of figure 3 displays the optical conductivity for the nine temperatures, eight in the normal state and one in the superconducting state. The optical conductivity can be written as  $\sigma(\omega) = -i\omega(\epsilon(\omega) - \epsilon_H)/4\pi$  where  $\epsilon_H$  is the dielectric constant at a high frequency ( $\sim 2 \text{ eV}$ ). At all temperatures we observe four sharp phonon modes out of the six infrared active phonon modes [30, 31, 32] expected for this polarization of the incident radiation. The phonons have been labelled P1 – P4 in the figure. We fitted the optical conductivity of these lines with a Drude-Lorentz model and found the line intensities to be temperature independent and of a magnitude expected for transverse optic (TO) phonons. Table I shows the parameters of the model.

The bottom panel of figure 3 shows the optical conductivity without the four phonon modes obtained through the subtraction of the fitted Drude-Lorentz conductivities from the measured conductivity. Several features stand out. First, there is a prominent onset of conductivity that appears at low temperature around  $400 \text{ cm}^{-1}$ . This feature is common to all cuprate superconductors and was identified early on as an onset of scattering from a bosonic mode [13, 14, 36]. Secondly, a strong peak at  $\approx 180 \text{ cm}^{-1}$ , designated S1, grows as the temperature is lowered. At lower frequencies, below  $150 \text{ cm}^{-1}$ ,

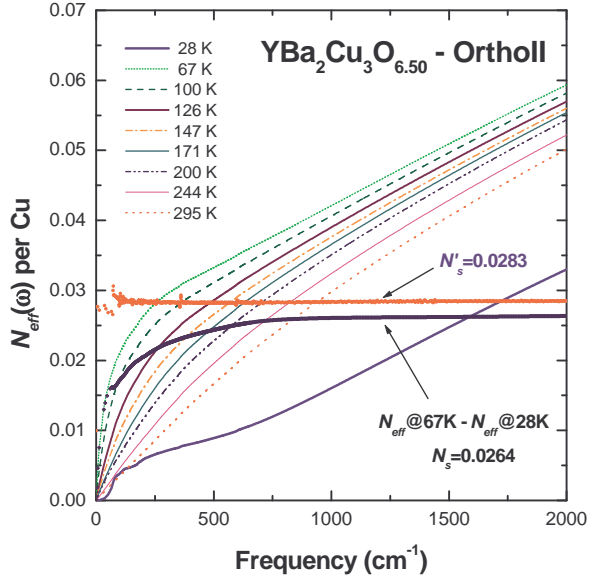


FIG. 4: The partial spectral weight up to  $2000 \text{ cm}^{-1}$  shown as dashed and solid curves. The spectral weight increases monotonically with temperature and frequency except for the 28 K curve (heavy solid curve) in the superconducting state where there is a loss of spectral weight to the condensate and the curve is sharply lowered. The curve marked  $N_s = N_{eff}(67K) - N_{eff}(28K)$  is an estimate of the spectral weight of the superconducting condensate. The curve marked  $N'_s$  is a plot of the condensate density obtained independently from the imaginary part of  $\sigma(\omega)$ .

there appears to be an additional strong absorption band, but any structure here must be interpreted with caution since they are derived from reflectance data close to unity which are subject to large systematic errors. Finally, at higher frequencies, there is a broad continuous background absorption that extends up to the plasma frequency and has been attributed to the influence of strong correlations [37, 38].

We define the effective number of carriers per copper atom in terms of the partial sum rule:  $N_{eff}(\omega) = \frac{2mV_{Cu}}{\pi e^2} \int_0^\omega \sigma_1(\omega') d\omega'$  where  $m$  is the free electron mass and  $V_{Cu}$  is the volume per copper atom,  $57.7 \text{ \AA}^3$ . Figure 4 shows  $N_{eff}(\omega)$  calculated from the optical conductivity. In the frequency region shown  $N_{eff}(\omega)$  increase uniformly with frequency and temperature in the normal state.

In the superconducting state at 28 K, shown in Figure 4 as a heavy solid curve, there is a dramatic loss of spectral weight due to the formation of the superconducting condensate. The effective number of carriers per copper atom in the condensate can be estimated from the partial sum rule by subtracting the normal state curve at 67 K from the superconducting curve at 28 K, also shown in the figure. The resulting difference curve rises rapidly at low frequency and saturates at a value of  $N_s = 0.0264$  above  $1000 \text{ cm}^{-1}$ . To find a better value of

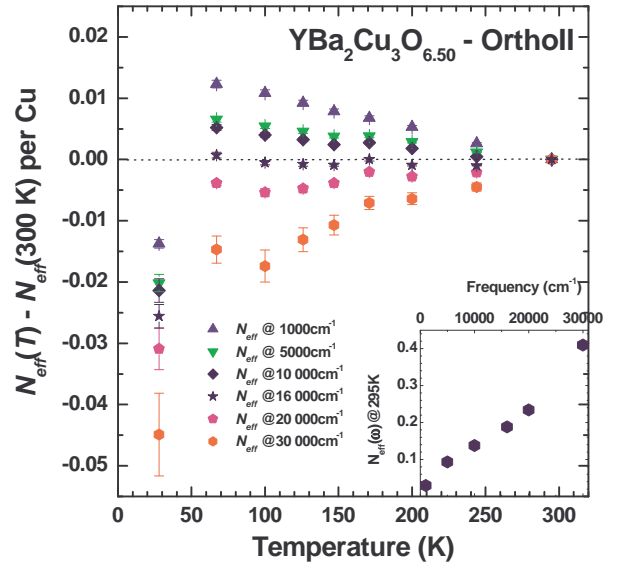


FIG. 5: The partial spectral weight integrated up to various frequencies as a function of temperature. Below  $16000 \text{ cm}^{-1}$  there is an increase in spectral weight as the temperature is lowered signaling a line narrowing on this frequency scale. Below  $T_c$  there is strong loss of spectral weight to the superconducting condensate. There is no evidence of any precursors to superconductivity at 67 K. In the inset we show  $N_{eff}(\omega)$  at 295 K.

$N_s$  we need to estimate the normal state curve at 28 K. We do this by extrapolating the temperature dependence in the normal state to 28 K (see Fig. 5). With the corrected value of  $N_{eff}$  at 28 K we get a more accurate value of  $N_s = 0.0276$ . The condensate density can also be estimated from the imaginary part of the conductivity provided the contribution from the residual conductivity is not included *i.e.*  $N'_s = \frac{mV_{Cu}}{4e^2} \omega [\sigma_2(\omega) - \sigma_{2r}(\omega)] = 0.0283$  where  $\sigma_{2r}$  is the residual quasiparticle conductivity in the superconducting state. Figure 4 shows both  $N_s$  and  $N'_s$  and it is clear that the two curves (when corrected) approach one another closely and the two methods differ by 2.5 % well within our 5 % estimated experimental error. There have been several reports of ab-plane spectral weight changes on entering the superconducting state, in other high  $T_c$  cuprates [39, 40, 41] at the 1 to 2 % level, but it should be noted that systematic errors in the absolute value of reflectance have a large influence on the magnitude of both  $N_s$  and  $N'_s$ , although the error of the *difference* is smaller. We estimate that our error in  $N_s$  and  $N'_s$  is 30 % but less than 5 % in the difference  $N'_s - N_s$ . Thus, at this point, we are unable to conclude from our data that there is evidence for any added or missing low frequency spectral weight when the superconducting state forms in the Ortho II Y123.

Figure 5 shows the temperature dependence of the partial spectral weight at various frequencies referred to the spectral weight at 300 K. We note that below 16 000

$\text{cm}^{-1}$  the spectral weight increases as the temperature is lowered while above this frequency there is a decrease. At  $16\,000\text{ cm}^{-1}$  the partial spectral weight is temperature independent. Since this frequency is close to our estimate of the limit of the free carrier conductivity, we conclude that there is a transfer of spectral weight to low frequencies as the temperature is lowered within the free carrier band on two frequency scales: a lower scale of the order of  $500\text{ cm}^{-1}$  shown by the spreading of the curves in Figure 4, and a higher one of the order of  $5000\text{ cm}^{-1}$  that is responsible for the temperature dependence below  $10\,000\text{ cm}^{-1}$  in Figure 5. We also note here that the temperature dependence of the partial spectral weight shows no sign of any precursors to superconductivity at  $67\text{ K}$  which is  $8\text{ K}$  above the bulk superconducting transition temperature.

The extended Drude model offers a detailed view of the charge carrier scattering spectrum and its contribution to the effective mass [42]. In this picture the scattering rate in the Drude expression is allowed to have a frequency dependence:

$$\begin{aligned}\sigma(\omega, T) &= i \frac{\omega_p^2}{4\pi} \frac{1}{\omega + [\omega\lambda(\omega, T) + i/\tau(\omega, T)]} \\ &= i \frac{\omega_p^2}{4\pi} \frac{1}{\omega - 2\Sigma_2^{op}(\omega, T)}\end{aligned}\quad (1)$$

where  $\omega_p$  is the plasma frequency,  $1/\tau(\omega, T)$  is the scattering rate and  $\lambda(\omega) + 1 = m^*(\omega)/m$ ,  $m^*(\omega)$  is an effective mass and  $m$  the bare mass. We also introduce the optical self energy  $\Sigma^{op} \equiv \Sigma_1^{op} + i\Sigma_2^{op}$ , where  $-2\Sigma_1^{op} = \omega\lambda(\omega, T)$  and  $-2\Sigma_2^{op} = 1/\tau$ . The optical self energy is, apart from a  $\cos(\theta) - 1$  factor, where  $\theta$  is a scattering angle, an average over the Fermi surface of the quasiparticle self-energy [16, 17, 43, 44] as measured by ARPES. Contrary to expectations, in optimally doped Bi-2212 where both optical and ARPES data exist, the self-energies derived from the two spectroscopies [45] are surprisingly similar to one another [15, 16, 18].

Figure 6 shows the scattering rate calculated from the extended Drude model where  $1/\tau(\omega, T) \equiv -2\Sigma_2^{op}(\omega, T) = \frac{\omega_p^2}{4\pi} \text{Re}\left(\frac{1}{\sigma(\omega, T)}\right)$  for Ortho II Y123. We also evaluate the real part of the optical self-energy, which is given by:  $-2\Sigma_1^{op}(\omega, T) = \omega\lambda(\omega, T) = -\frac{\omega_p^2}{4\pi} \text{Im}\left(\frac{1}{\sigma(\omega, T)}\right) - \omega$  and is shown in Figure 8. For the calculation of the optical self-energy and the scattering rate we need a value for the plasma frequency which includes spectral weight up to the interband transitions. Using a procedure adopted in a previous study [46] we find a plasma frequency  $\omega_p = 15\,110\text{ cm}^{-1}$ .

In Fig. 6 we see an overall increase in scattering both with temperature and frequency. The frequency dependence is monotonic with two thresholds, shown with arrows, where the scattering rate undergoes a step-like increase, a prominent low frequency one at  $400\text{ cm}^{-1}$  and

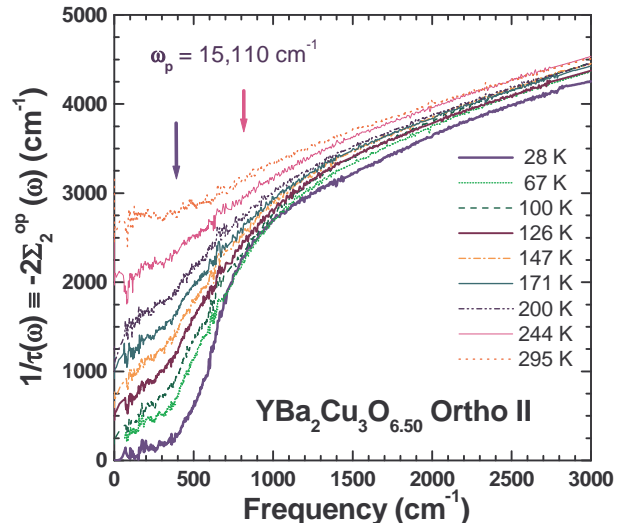


FIG. 6: The optical scattering rate obtained from the extended Drude model. Two onsets, denoted by arrows dominate the scattering.

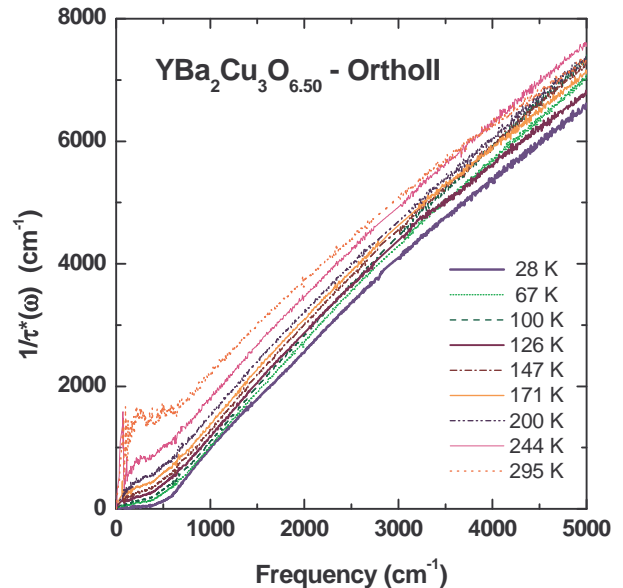


FIG. 7: The optical effective scattering rate. Given by the ratio of the real and imaginary parts of the conductivity times the frequency, this quantity has a linear frequency dependence that extends to very high frequencies and a temperature dependence that does not vary much with frequency.

a weaker, higher frequency one at  $850\text{ cm}^{-1}$ . The variation of the scattering rate with temperature is roughly linear at low frequency, but becomes much weaker at high frequency above the high frequency threshold. The scattering rate is larger than the frequency at all temperatures except at  $28\text{ K}$  in the superconducting state, *i.e.*  $\hbar/\tau > \hbar\omega$ .

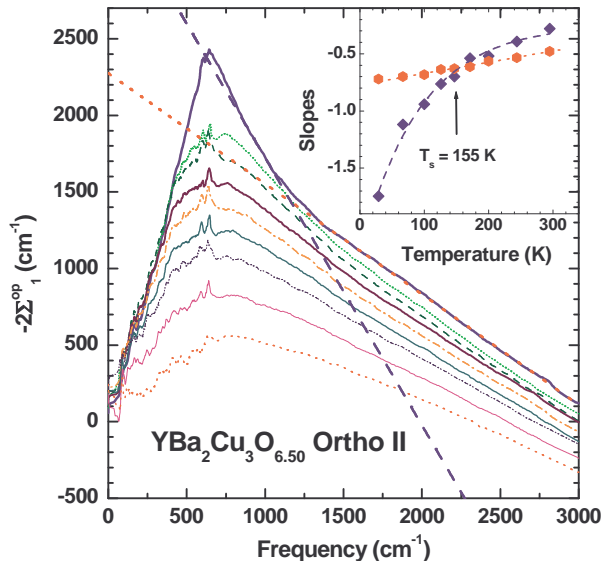


FIG. 8: The optical self-energy. The imaginary part of the scattering rate is plotted. A broad peak is seen at 295 K (the lowest curve). As the temperature is lowered this peak splits into two components with a sharp peak appearing below 175 K as shown by the curvature change at this temperature. The inset shows a curvature analysis of the self-energy where the slope of the self-energy in the two regions, shown in the main panel as two dashed lines, have been plotted, circles, high frequency and diamonds, low frequency.

Fig. 7 shows the *effective* optical scattering rate defined as:

$$\frac{1}{\tau^*(\omega, T)} = \omega \frac{\sigma_1(\omega, T)}{\sigma_2(\omega, T)} \quad (2)$$

One advantage of this quantity is that to calculate it the plasma frequency is not needed. This quantity is also more linear with frequency than the optical scattering rate [47].

In Fig. 8 we show the real part of the optical self-energy. It is related by Kramers-Kronig transformations to the scattering rate shown in Fig. 6. The separation of the two components of scattering is less obvious in this plot but in analogy with the Bi-2212 system where we have investigated the detailed doping dependent data on this quantity [16], we find that the bosonic mode gives rise to a peak on top of a broader background. With increased underdoping in Bi-2212 the peak becomes triangular and harder to resolve from the background and is very similar in appearance to the Ortho II Y123 data shown here. We can attempt to resolve the peak by focusing on the break in slope that occurs between 1000  $\text{cm}^{-1}$  and 1400  $\text{cm}^{-1}$  in the temperature range from 28 K to 171 K. Above 200 K the break in slope cannot be resolved. The inset to Fig. 8 shows a plot of the slopes of two straight dashed lines that have been fitted to the experimental data above and below the break frequency.

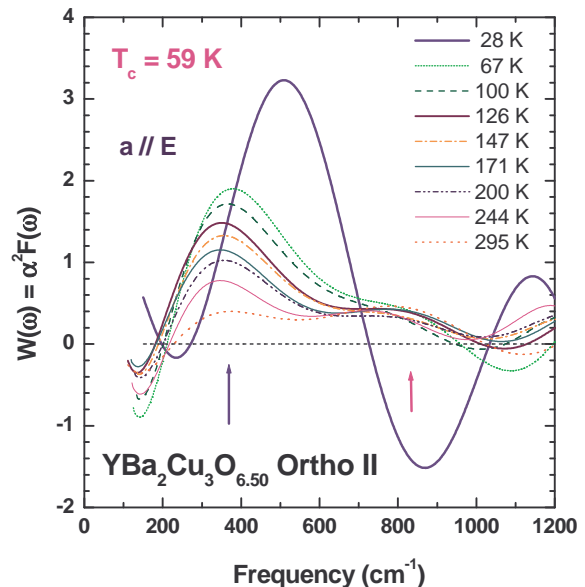


FIG. 9: The Eliashberg function,  $\alpha^2 F(\omega) \approx W(\omega)$ , which is calculated by using the Eq. 3. We observe two peaks: one is temperature dependent at lower frequency and the other is temperature independent at higher frequency. In the superconducting state there is a large shift of the low energy peak and a dramatic overshoot of the scattering rate giving rise to a negative contribution to the Eliashberg function.

We find that a plot of the two slopes shows that they cross at 155 K, *i.e.* the second derivative of the optical self-energy goes through zero at this temperature. This is shown in the inset to Fig. 8

Recent calculations [21] of the self-energy of the charge carriers interacting with collective spin excitations suggest that the self-energy acquires an S-shaped frequency dependence in the presence of a sharp mode, whereas in the absence of such a mode the curve has a monotonically negative second derivative. From these observations we conclude, as a first approximation, that the bosonic mode is confined to temperatures below 155 K.

For another estimate of the strength of the interaction of the charge carriers with the sharp mode we used the procedure introduced by Marsiglio *et al.* [15, 36, 48] where the bosonic spectral function is derived from the second derivative of the optical scattering rate. This function can be written as follows [36, 42, 49]:

$$W(\omega) \equiv \frac{1}{2\pi} \frac{d^2}{d\omega^2} \left[ \frac{\omega}{\tau(\omega)} \right] \quad (3)$$

and  $W(\omega) \approx \alpha^2 F(\omega)$  at zero temperature in the normal state, where  $\alpha$  is a coupling constant, and  $F(\omega)$  is a bosonic density of states. The results are shown in Fig. 9. The normal state shows two broad peaks; a prominent one at  $\approx 350 \text{ cm}^{-1}$  and a much weaker one at  $\approx 800 \text{ cm}^{-1}$ . The higher frequency peak does not change with

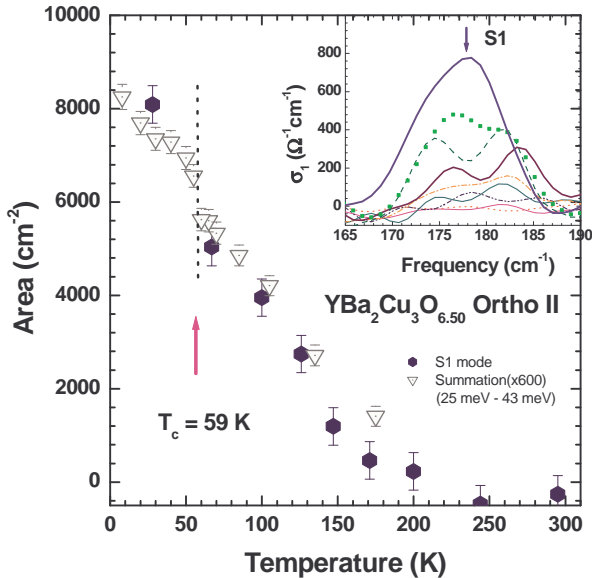


FIG. 10: Area under the S1 mode as a function of temperature. We also show the area under the neutron resonance peak [27] at  $Q = (1/2, 3/2, 2.2)$  and 33.1 meV, solid triangles from 25 to 43 meV (open triangles) as a function of temperature.

temperature while the lower frequency one grows monotonically as temperature decreases. Another interpretation is in terms of a temperature dependent peak and a temperature independent background, four times lower in amplitude. In the superconducting state there is a dramatic shift of the lower peak to higher frequency and the development of a region of negative spectral function  $W(\omega)$  between 700 and 1000  $\text{cm}^{-1}$ . This behavior has been predicted by Abanov *et al.* [48].

Fig. 10 shows the area under the peak S1 as a function of temperature obtained from a fit of a Lorentzian function to the conductivity peak. We see that the intensity of this feature decreases linearly with temperature going to zero at  $\approx 200$  K. On the same graph we have plotted the area under the neutron resonance and it is clear that the two phenomena have parallel temperature dependencies. We note that the spectral weight of the S1 peak,  $8000 \text{ cm}^{-2}$  represents only 0.006 % of the total free carrier spectral weight,  $1.25 \times 10^8 \text{ cm}^{-2}$ .

We note that to obtain a finite frequency absorption peak such as the peak S1, we need to break translational symmetry of the charge carriers. We can rule out phonon absorption which would be inconsistent with the large spectral weight of the peak S1 and the fact the spectral weight is temperature dependent as shown in Fig 10. There are a number of possible candidate mechanisms but we would like to focus on the static charge-density patterns seen by scanning probe microscopy in Bi-2212 [50, 51]. Models for optical absorption by strip-like patterns have been described by Benfatto and Morais

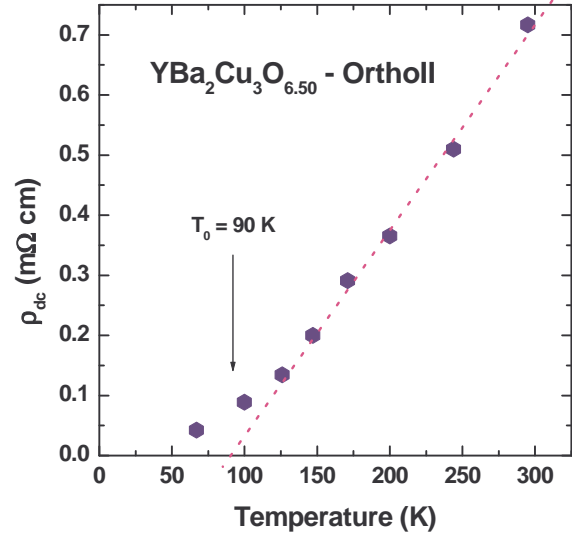


FIG. 11: DC resistivity extracted from the optical conductivity by extrapolating the optical conductivity to zero frequency. The temperature dependence shows the familiar linear variation with an intercept on the temperature axis of  $\approx 90$  K.

Smith [10]. The model describes the optical absorption by charges confined by a static pinning potential with two parameters, the strength of the potential and the modulation amplitude.

Finally, we show the calculated dc resistivity extracted from the extrapolated zero frequency limit of the optical conductivity. Figure 11 shows the resulting dc resistivity for the eight normal state temperatures. The resistivity shows the familiar linear temperature dependence with an intercept on the temperature axis of 90 K, typical of underdoped samples of high  $T_c$  cuprates. A more detailed comparison shows some discrepancies with the best dc transport data [52]. First, our absolute value of the resistivity at 300 K is  $0.7 (\text{m}\Omega\text{cm})^{-1}$  while Ando *et al.* find, at the same doping level, a resistivity of  $1.0 (\text{m}\Omega\text{cm})^{-1}$ . The second difference is the value of the resistivity in the low temperature plateau region just above  $T_c$  where Ando *et al.* measure a residual resistivity of about  $200 (\mu\Omega\text{cm})^{-1}$  whereas our extrapolation yields less than  $50 (\mu\Omega\text{cm})^{-1}$ . We think this difference may originate in the more ordered chain layer in our samples which were annealed whereas the sample of Ando *et al.* were quenched and presumably more disordered. The lower absolute value of the 300 K resistivity is harder to understand since we don't expect inelastic scattering, a mechanism responsible for the high temperature resistivity, to depend on disorder. One often suspects contact geometry in dc transport but as Ando *et al.* have shown, errors from those sources amount to at most a few percent in their data. Where the two data sets are in good

agreement is the value of  $\approx 90$  K for the intercept on the temperature axis.

## DISCUSSION

We now turn to a general interpretation of our data in terms of models proposed for the electrodynamics of cuprates focusing our attention on the low frequency spectral region below the free carrier plasma edge  $\approx 10\,000\text{ cm}^{-1}$ . It is clear from even the most superficial view of the data that the optical properties shown here are not those of a set of free carrier interacting weakly with impurities through elastic scattering or with lattice vibrations through inelastic scattering. Two approaches have been used to account for these deviations, the one and the two component models of conductivity. In the one component model any deviation from the simple Drude formula are attributed to a single set of charge carriers interacting with a variety of bosonic excitations while in the two component model a low frequency Drude component is separated by curve fitting and any remaining absorption is attributed to a mid-infrared band.

There is ample evidence that many conducting oxides do have a separate well-defined mid-infrared band with a peak frequency that moves to lower frequencies with doping [53]. This is also true of the one-layer cuprates, in particular  $\text{La}_{2-x}\text{Sr}_x\text{CuO}_4$  [54]. In some materials, when the peak reaches zero frequency, striking changes occur in the transport properties, for example,  $\text{Ba}_{1-x}\text{K}_x\text{BiO}_3$  becomes superconducting at this doping level [55]. Recent evidence from thermal conductivity suggests that  $\text{La}_{2-x}\text{Sr}_x\text{CuO}_4$  becomes an insulator below a doping level of 0.06 where superconductivity also sets in whereas Y123 remains in the conducting pseudogap state well below the doping level [56] of the superconductivity boundary. These observations suggest that the one-component to two-component transition occurs at different doping levels for these two materials and that the Y123 system remains metallic to the lowest doping levels. We conclude that, at least at the level of doping of ortho-II Y123, we are justified in using the one-component model.

The striking result of the one-component model is the strong frequency dependent scattering rate  $1/\tau(\omega, T)$  shown in Fig 6. There is a nearly perfect linear variation of scattering at high frequency with a strong threshold at  $400\text{ cm}^{-1}$  at low temperatures that gradually washes with increasing temperature. We will interpret our spectra within the one-component model in terms of a scattering rate that is averaged over the Brillouin zone and is the sum of two frequency dependent terms, a bosonic mode that dominates at low temperature but whose spectral weight weakens as the temperature rises and a featureless temperature independent background that extends to high frequencies.

Several theoretical models of strongly correlated sys-

tem have been evoked to explain the strong linearly rising frequency dependent scattering rate. Earlier models included the Marginal Fermi Liquid [57], the Nested Fermi Liquid models [58], the Nearly Antiferromagnetic Liquid [38, 59], and the Luttinger Liquid model [37]. All models predict a continuous linear rise of scattering governed by an energy scale of the order of  $\approx 0.5\text{ eV}$ . The large energy scale rules out a simple phonon mechanism for the broad background scattering which would predict a flattening of the scattering rate beyond the maximum phonon frequency [17]. The strongly temperature dependent threshold has generally been interpreted in terms of coupling to a bosonic mode [13, 14], in particular the the 41 meV magnetic resonance [15, 16, 17].

### Bosonic Mode Analysis of the Optical Scattering Rate

Here we will adopt the approach of Schachinger *et al.* [17] and treat both the mode and the continuum scattering on an equal basis assuming that *both* originate from coupling of the charge carriers to bosonic fluctuations.

To study the temperature dependence of the coupling of bosonic modes to charge carriers we used the following expression to model the scattering rate within the extended Drude formalism:

$$\frac{1}{\tau(\omega, T)} = \frac{\pi}{\omega} \int_0^{+\infty} d\Omega \alpha^2 F(\Omega) \int_{-\infty}^{+\infty} dz [N(z - \Omega) + N(-z + \Omega)] [n_B(\Omega) + 1 - f(z - \Omega)][f(z - \omega) - f(z + \omega)] \quad (4)$$

where  $\alpha^2 F(\Omega)$  is the bosonic spectral function [60],  $N(z)$  is the normalized density of state of the quasiparticles,  $n_B(\Omega) = 1/(e^{\beta\Omega} - 1)$ ,  $f(z) = 1/(e^{\beta z} + 1)$  are the boson and fermion occupation numbers, respectively, and  $\beta = 1/(k_B T)$ .

Eq. 4 represents a finite temperature generalization of the  $T = 0$  expression [61],

$$\frac{1}{\tau(\omega)} = \frac{2\pi}{\omega} \int_0^{\omega} d\Omega \alpha^2 F(\Omega) \int_0^{\omega - \Omega} dz \frac{1}{2} [N(z) + N(-z)] \quad (5)$$

Eq. 4 is derived using the method proposed by Shulga *et al.* [62] and its derivation will be given elsewhere [63]. Both Eq. 4 and 5 are suitable for the case when the quasiparticle density of states,  $N(z)$ , cannot be taken as constant in the vicinity of the Fermi levels, *e.g.* in the pseudogap state.

The density of state  $N(z)$  was modelled with a pseudogap with a quadratic gap function:

$$N(z) = [N(0) + (1 - N(0)) \frac{z^2}{\Delta^2}] \theta(\Delta - |z|) + \theta(|z| - \Delta) \quad (6)$$



where  $1 - N(0)$  is the depth of the gap,  $\theta(z)$  is the Heaviside step function, and  $\Delta = 350 \text{ cm}^{-1}$  is the frequency width of the gap based on spectroscopic data for the pseudogap from tunneling [64], and  $c$ -axis infrared conductivity [65]. An example for a depth of the gap of 0.50 is shown in Fig. 13.

For the bosonic spectral function  $\alpha^2 F(\Omega)$  we used the sum of two functions, a peak and a background.

$$\alpha^2 F(\Omega) = \text{PK}(\Omega) + \text{BG}(\Omega) \quad (7)$$

$$\text{PK}(\Omega) = \frac{A}{\sqrt{2\pi}(d/2.35)} e^{-(\Omega - \Omega_{PK})^2 / [2(d/2.35)^2]} \quad (8)$$

$$\text{BG}(\Omega) = \frac{I_s \Omega}{\Omega_0^2 + \Omega^2} \quad (9)$$

where  $\text{PK}(\Omega)$  is a Gaussian peak and  $\text{BG}(\Omega)$  is the background which we have modelled on the spin fluctuation spectrum of Millis, Monien, and Pines (MMP) [38].  $A$  is the area under the Gaussian peak,  $d$  is the full width at half maximum (FWHM), and  $\Omega_{PK}$  is its center frequency. We fixed the parameters of the Gaussian peak to values shown in Table II based on the inelastic neutron scattering results of Stock *et al.* [66].  $I_s$  is the intensity of the MMP background and  $\Omega_0$  is the frequency of the background at maximum. The complete bosonic spectral function  $\alpha^2 F(\Omega)$  used is shown in Fig. 12. It has two adjustable parameters, the amplitude of the Gaussian peak  $A$  and depth of the pseudogap  $1 - N(0)$ . All the other parameters have been determined from other experiments.

We used least squares to fit our scattering rate data shown in Fig. 6 to Eq. 4. The amplitude of the MMP background and its center frequency were determined by fitting the data at 295 K including only the MMP background in  $\alpha^2 F(\Omega)$  with a very shallow gap (see Table II) in the Fermion density of states  $N(z)$ . We fixed the background parameters for all other lower temperatures to their 295 K values. For further fits at lower temperatures, only two free parameters were used: the depth of the gap in the density of states and the area under the resonance peak,  $A$ . The calculated  $1/\tau(\omega)$  spectra are compared with the measured data in Fig 15. The dimensionless coupling constant or mass enhancement factor  $\lambda$  is defined as:

$$\lambda = 2 \int_0^\infty d\Omega \frac{\alpha^2 F(\Omega)}{\Omega}. \quad (10)$$

The contributions to  $\lambda_{PK}$  and  $\lambda_{BG}$ , from the peak and the background as well as other parameters of the model are shown in the Table II.

One result of our fit is the temperature dependence of the depth of the pseudogap shown in the lower panel of Fig. 13. The depth, we find, corresponds to a 41 % depression of the density of states at low temperature decreasing gradually to 17 % at room temperature. The

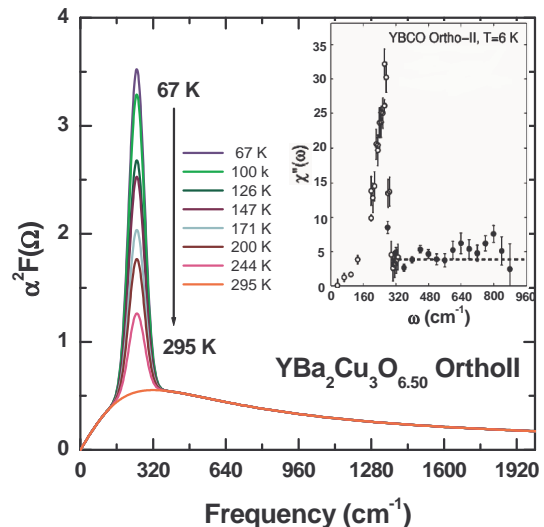


FIG. 12: The bosonic spectral function  $\alpha^2 F(\Omega)$  obtained from the least square fits to the experimental data. In the inset we show  $\chi''(\omega)$  determined by neutron scattering from Fig. 14 in Ref. [66].

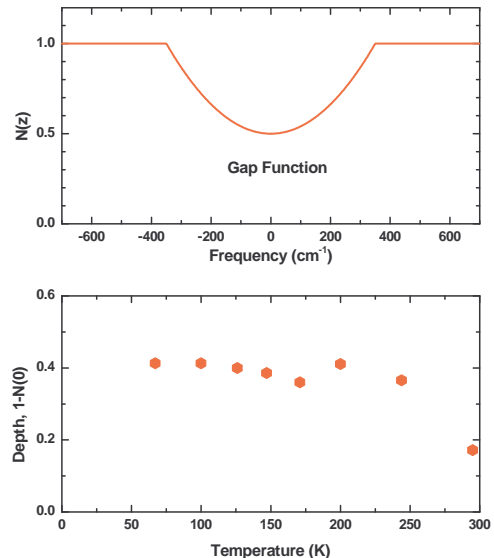


FIG. 13: The upper panel shows the quasiparticle density of state with a gap,  $N(z)$ . The lower panel shows the depth of the pseudogap for the least square fits. The other parameters of the fit are shown in Table II.

depth of the pseudogap in the  $c$ -axis optical conductivity is more pronounced [65] but it is known that  $c$ -axis transport is weighted more heavily in the antinodal direction where the pseudogap is deeper whereas  $ab$ -plane transport is more evenly distributed in momentum space.

Next, we compare our spectral function  $\alpha^2 F(\Omega)$  in Fig. 12 with the magnetic susceptibility  $\chi''(\omega)$  determined by neutron scattering at 6 K ( $< T_c$ ) by Stock *et al.* (see inset in Fig. 12). The two sets of curves are very similar although it should be pointed out that our data are in the normal states and neutron data are in the superconducting state and that the *width* of our mode has

been set equal to that of the neutron resonance mode.

Comparing the relative amplitudes of the peak and the background, we find a substantial difference with the neutron data. For the ratio of the background to the peak amplitude our  $\alpha^2 F(\Omega)$  at 67 K gives  $\sim 0.17$  while the neutron  $\chi''(\omega)$  gives  $\sim 0.27$  in the normal state (we estimated the ratio in the normal state from the temperature dependent intensity of the neutron mode [27]). The relative amplitude of the peak in our spectra is 63 % stronger than what is seen by neutron scattering. In the absence of a more detailed calculation of the spectral function, this discrepancy is not surprising since the coupling of the charge carriers to spin fluctuations involves integrations over the Fermi surface and we are reporting only on weighted averages. On the other hand our data leaves open the possibility that the high frequency channel of conductivity, that is active in producing our background, is not well described by the MMP spin fluctuations. In addition to the relative amplitudes we can also compare the areas under the peak and background spectral functions. There is a sum rule for the area under  $\chi''(\omega)$  which is related to our optical function  $\alpha^2 F(\Omega)$  by a coupling constant,  $g^2$ . Neutron scattering finds that the area under the spin resonance is about 3 % of the total area. In our case at 67 K this fraction is about 25 %, considerably larger. It can be argued that the coupling to the resonance  $g^2$  could be larger than its background value by a factor of  $\sim \sqrt{8}$ . This is reasonable since the resonance is around  $(\pi, \pi)$  where the susceptibility is also expected to peak.

temp. (K)	peak				MMP			depth $1 - N(0)$
	$A$	$\Omega_{PK}$	$d$	$\lambda_{PK}$	$I_s$	$\Omega_0$	$\lambda_{BG}$	
67	255	248	80	2.20	354	320	3.30	0.413
100	235	248	80	1.93	354	320	3.30	0.413
147	170	248	80	1.40	354	320	3.30	0.386
200	105	248	80	0.86	354	320	3.30	0.411
244	62	248	80	0.51	354	320	3.30	0.366
295	0	248	80	0.00	354	320	3.30	0.172

TABLE II: The parameters of the bosonic mode analysis at six representative temperatures,  $T = 67$  K, 100 K, 147 K, 200 K, 244 K, and 295 K. The peak is a Gaussian function (see Eq. 8) and MMP is the background (see Eq. 9). The quantities  $\lambda_{PK}$  and  $\lambda_{BG}$  are the coupling constants for the peak and the MMP background, respectively. The depth,  $1 - N(0)$ , is the depth of the gap at Fermi level in the density of state. All the frequencies are measured in  $\text{cm}^{-1}$ .

In Fig. 16 we compare three quantities: the total area under the magnetic susceptibility in the 25 to 43 meV energy range from Stock *et al.* [27], the area under the peak at  $350 \text{ cm}^{-1}$  in the  $W(\Omega) \approx \alpha^2 F(\Omega)$  obtained from the second derivative of  $1/\tau(\omega)$ , and the area under the peak at  $248 \text{ cm}^{-1}$  in the  $\alpha^2 F(\Omega)$  from our fit. We note that the two areas from the two different procedures for deriving  $\alpha^2 F(\Omega)$  show almost identical temperature de-

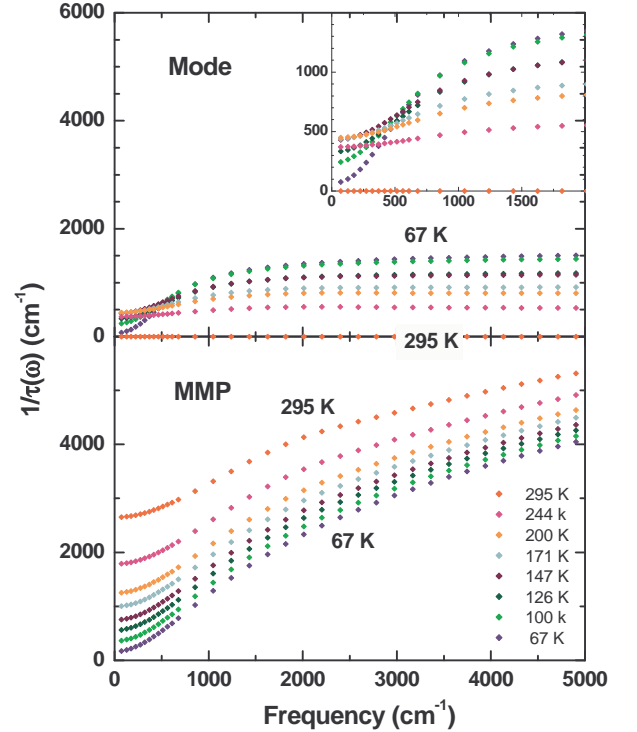


FIG. 14: The mode contribution (upper panel) and the MMP back ground contribution (lower panel) on the scattering rate based on Eq. 4 with the parameter shown in Table II and pseudogap information of Fig 13 for the normal states. We note at high frequencies the opposite temperature dependencies of the mode and the background contributions.

pendencies. The area under the peak obtained from the magnetic susceptibility shows a temperature trend similar to those of the optical data.

## DISCUSSION AND CONCLUSIONS.

### The two channels of scattering of the charge carriers

In analyzing the optical properties of Ortho II Y123 we have adopted the one-component model of conductivity, attributing any deviations from the simple Drude formula to inelastic processes. We find that the high frequency processes are well described by the MMP spectrum of spin fluctuations with a temperature dependence that originates in the bosonic occupation numbers, but a temperature *independent* spectral function, while at lower frequencies a strong temperature dependence sets in and the conductivity is well described by the extended Drude model with a temperature *dependent* spectral function.

The two methods we used to estimate the shape and temperature dependence of the bosonic spectrum gave very similar results. The main contribution to the spectral weight came from a prominent peak at  $350 \text{ cm}^{-1}$

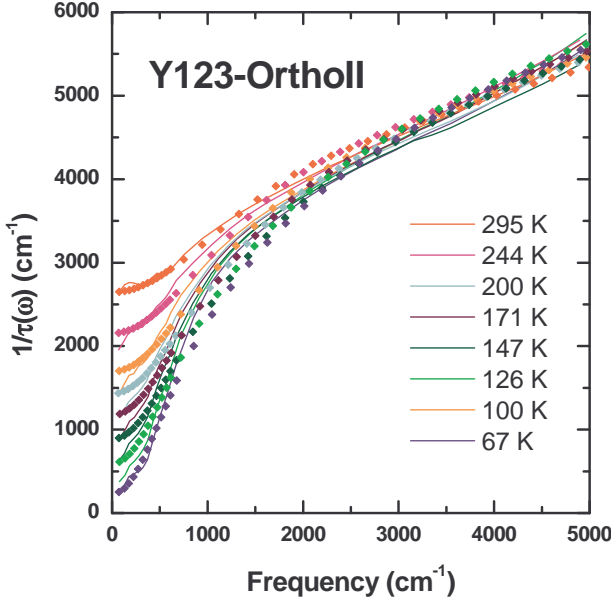


FIG. 15: The optical scattering rates (solid lines) and our fits (symbols) based on Eq. 4 with the bosonic spectral function shown in Fig. 12 and pseudogap information of Fig. 13 for the normal states. We note that the negative temperature dependence of the mode contribution combined with the almost equal and opposite contribution of the background results in a nearly temperature independent scattering rate at high frequencies, in complete agreement with the experimental results.

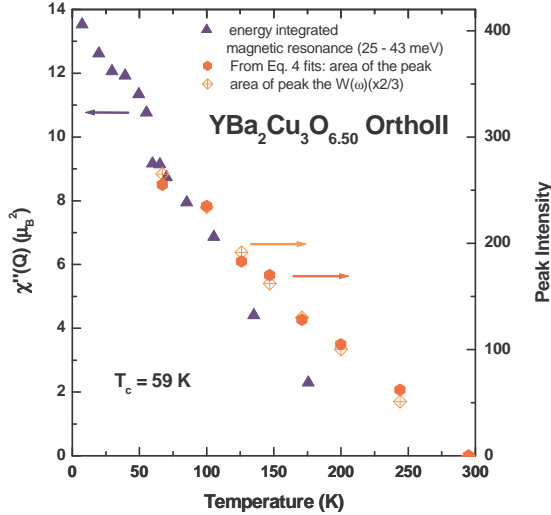


FIG. 16: Temperature dependence of the amplitude of the sharp mode. The open diamonds with cross are from the second derivative analysis of the scattering rate, the closed hexagons are from fit a scattering rate to the model including a sharp mode and a background. The upright triangles show the energy integrated amplitude of the neutron mode Stock *et al.* [27].

which was strongly temperature dependent in strength. From this temperature dependence we identified the mode with the neutron resonance which has a frequency of  $248 \text{ cm}^{-1}$ . The  $100 \text{ cm}^{-1}$  discrepancy we attributed to the effect of the pseudogap in the density of states which, as calculations suggest, has the effect of shifting upward the frequency of any bosonic mode. To fit the data, the strength of the mode had to be temperature dependent and the electronic density of states had to have a gap whose depth was also temperature dependent. These observations are in accord with what is known about the normal state of underdoped Y123 from other experiments.

The properties of the sharp bosonic resonance in the infrared scattering rate agree with the properties of the  $(\pi, \pi)$  spin-flip neutron resonance mode. The frequency of the bosonic resonance  $248 \text{ cm}^{-1}$  or  $31 \text{ meV}$  agrees with the frequency of the neutron mode measured by Stock *et al.* [27] (provided the pseudogap is included in the model). The temperature dependence of the strength of the mode also agrees with the neutron measurements on Ortho II Y123 samples from the same source. The total spectral weight of the mode determined from least squares fits drops monotonically with temperature and reaches zero between 200 and 300 K, in agreement with the spectral weight of the neutron mode.

Fig 14 shows separately the two contributions to the scattering rate. We see that the combination of a sharp mode whose strength decreases with temperature and a temperature independent background solves a long standing problem in the optical conductivity of the cuprates: there is a strong temperature dependence at low frequencies but above  $500 \text{ cm}^{-1}$  the scattering is nearly temperature independent. In the picture of mode and background, both caused by coupling to bosons, this high frequency behavior is the result of a competition between a rising absorption due to occupancy of the background boson population and a decrease in the strength of the bosonic mode with temperature. This scenario predicts an overall linear temperature dependence at all frequencies above the temperature where the sharp mode disappears. There is some evidence for this kind of behavior in the data for  $\text{La}_{2-x}\text{Sr}_x\text{CuO}_4$  which does not have a magnetic resonance but shows a linear temperature dependence characteristic of bosons both in the dc resistivity [67] and optical scattering rate at high frequency [68].

## Summary and conclusion

In summary, we have shown that two optical phenomena in Ortho II Y123 have a close association with the magnetic resonance as measured for samples from the same source. The first is the onset of scattering associated with a bosonic resonance. This has been suggested by several previous investigators [15, 16, 17, 20], but here,

for the first time we base our conclusions on experiments that use crystals with the same, well-defined doping level grown by the same technique.

The second is the low-temperature conductivity peak that we have designated S1. Its connection to the magnetic resonance is not obvious since the magnetic resonance by itself is not optically active. One possible mechanism is the growth of in-plane coherence that takes place in this temperature region and has been suggested to be the closely related to the transverse plasma resonance that is seen in interplane conductivity [69]. The peak S1 may be such a resonance associated with in-plane charge density modulations either through pinning to defects [10] or through a transverse plasma resonance associated with the inhomogeneous charge density that seems to be present in underdoped cuprates in the normal state [50, 51].

This work has been supported by the Canadian Natural Science and Engineering Research Council and the Canadian Institute of Advanced Research. We would like to thank Artem Abanov, Elena Banscones, Dimitri Basov, Lara Benfatto, Andrey Chubukov, Chris Homes, Peter Johnson, Alexandra Lanzara, Boza Mitrovic, Mike Norman, the late Brian Statt, Setsuko Tajima, David Tanner, Tony Valla, and Zara Yamani, for helpful discussions.

---

\* Electronic address: hwangjs@mcmaster.ca

- [1] For a review see: T. Timusk and B. Statt, Rep. Prog. Phys. **62**, 61 (1999); an update to this review can be found in T. Timusk, Solid State Commun. **127**, 337 (2003).
- [2] J. Rossat-Mignod, L.P. Regnault, C. Vettier, P. Bourges, P. Burlet, J. Bossy, J.Y. Henry, and G. Lapertot, Physica C **185-189**, 86 (1991).
- [3] H.A. Mook, Pengcheng Dai, S.M. Hayden, G. Aeppli, T.G. Perring, and F. Do, Nature (London) **395**, 580 (1998).
- [4] H.F. Fong, P. Bourges, Y. Sidis, L.P. Regnault, A. Ivanov, G.D. Gu, N. Koshizuka, and B. Keimer, Nature (London) **398**, 588 (1999).
- [5] Z.A. Xu, N.P. Ong, Y. Wang, T. Kakeshita, and S. Uchida, Nature (London) **406**, 486 (2000).
- [6] N.P. Ong, Y. Wang, S. Ono, Y. Ando, and S. Uchida, Ann. der Physik **13**, 9 (2004).
- [7] J.M. Tranquada, B.J. Sternlieb, J.D. Axe, Y. Nakamura, and S. Uchida, Nature (London) **375**, 561 (1995).
- [8] M. Dumm, D.N. Basov, S. Komiya, Y. Abe, and Y. Ando, Phys. Rev. Lett. **88**, 147003 (2002).
- [9] A. Lucarelli, S. Lupi, M. Ortolani, P. Calvani, P. Maselli, M. Capizzi, P. Giura, H. Eisaki, N. Kikugawa, T. Fujita, M. Fujita, and K. Yamada, Phys. Rev. Lett. **90**, 037002 (2003).
- [10] L. Benfatto and C.M. Smith, Phys. Rev. B **68**, 184513 (2003).
- [11] V.J. Emery and S.A. Kivelson, Nature (London) **374**, 434 (1995).
- [12] J. Corson, R. Malozzi, J. Orenstein, J.N. Eckstein, and I. Bozovic, Nature **398**, 221 (1999).
- [13] G.A. Thomas, J. Orenstein, D.H. Rapkine, M. Capizzi, A.J. Millis, R.N. Bhatt, L.F. Schneemeyer, and J.V. Waszczak, Phys. Rev. Lett. **61**, 1313 (1988).
- [14] A.V. Puchkov, D.N. Basov, and T. Timusk, J. Physics: Condensed Matter, **8**, 10049 (1996).
- [15] J. P. Carbotte, E. Schachinger, and D.N. Basov, Nature **401**, 354 (1999).
- [16] J. Hwang, T. Timusk, and G.D. Gu, Nature (London) **427**, 714 (2004).
- [17] E. Schachinger, J.J. Tu, and J.P. Carbotte, Phys. Rev. B **67**, 214508 (2003).
- [18] M.R. Norman and H. Ding, Phys. Rev. B **57**, R11089 (1998).
- [19] M. Eschrig and M.R. Norman, Phys. Rev. B **67**, 144503 (2003).
- [20] P.D. Johnson, T. Valla, A.V. Fedorov, Z. Yusof, B.O. Wells, Q. Li, A.R. Moodenbaugh, G.D. Gu, N. Koshizuka, C. Kendziora, S. Jian, and D.G. Hinks, Phys. Rev. Lett. **87**, 177007 (2001).
- [21] A.V. Chubukov and M.R. Norman, Phys. Rev. B **70**, 174505 (2004).
- [22] J.F. Zasadzinski, L. Ozyuzer, N. Miyakawa, K.E. Gray, D.G. Hinks, and C. Kendziora, Phys. Rev. Lett. **87**, 067005 (2001).
- [23] A. Lanzara, P.V. Bogdanov, X.J. Zhou, S.A. Kellar, D.L. Feng, E.D. Lu, T. Yoshida, H. Eisaki, A. Fujimori, K. Kishio, J.-I. Shimoyama, T. Noda, S. Uchida, Z. Hussain, Z.-X. Shen, Nature (London) **412**, 510 (2001).
- [24] H.Y. Kee, S.A. Kivelson, and G. Aeppli, Phys. Rev. Lett. **88**, 257002 (2002).
- [25] Ruixing Liang, D.A. Bonn, and Walter N. Hardy, Physica C **336**, 57 (2000).
- [26] Z. Yamani, W.A. MacFarlane, B.W. Statt, D. Bonn, R. Liang, and W.N. Hardy, cond-mat/0310255.
- [27] C. Stock, W.J.L. Buyers, R. Liang, D. Peets, Z. Tun, D. Bonn, W.N. Hardy, and R.J. Birgeneau, Phys. Rev. B **69**, 014502 (2004).
- [28] Ruixing Liang, D.A. Bonn, W.N. Hardy, Physica C **304**, 105 (1998).
- [29] C.C. Homes, M.A. Reedyk, D.A. Crandles, and T. Timusk, Appl. Opt. **32** 2976 (1993).
- [30] M.K. Crawford, G. Burns, and F. Holtzberg, Solid State Commun. **70**, 557 (1989).
- [31] S. Tajima, T. Ido, S. Ishibashi, T. Itoh, H. Eisaki, Y. Mizuo, T. Arima, H. Takagi, and S. Uchida, Phys. Rev. B **43**, 10496 (1991).
- [32] C.C. Homes, A.W. McConnell, B.P. Clayman, D.A. Bonn, Ruixing Liang, W.N. Hardy, M.Inoue, H. Negishi, P. Fournier, and R.L. Greene, Phys. Rev. Lett. **84**, 5391 (2000).
- [33] T. Pereg-Barnea, P.J. Turner, R. Harris, G.K. Mullins, J.S. Bobowski, M. Raudsepp, Ruixing Liang, D.A. Bonn, and W.N. Hardy, Phys. Rev. B **69**, 184513 (2004).
- [34] Frederick Wooten, *Optical Properties of Solids*, Academic, New York (1972).
- [35] H. Romberg, N. Nücker, J. Fink, Th. Wolf, X.X. Xi, B. Koch, H.P. Geserich, M. Dürller, W. Assmus, and B. Gegenheimer, Z. Phys B **78**, 367 (1990).
- [36] F. Marsiglio, T. Startseva, and J.P. Carbotte, Phys. Lett. A **245**, 172 (1998).
- [37] P.W. Anderson, Phys. Rev. B **55** 11785 (1997).
- [38] A.J. Millis, H. Monien, and D. Pines, Phys. Rev. B **42**,

- 167 (1990).
- [39] D.B. Tanner, Y.-D. Yoon, A. Zibold, H.L. Liu, M.A. Quijada, S.W. Moore, J.M. Graybeal, B.-H.O. J.T. Markert, R.J. Kelley, M. Onellion, and J.-H. Cho, in *Spectroscopic Studies of Superconductors*, Ivan Bozovic, Dirk van der Marel, Editors, Proc. SPIE 2696, 13, (1996).
- [40] A.F. Santander-Syro, R.P.S.M. Lobo, N. Bontemps, Z. Konstantinovic, Z.Z. Li, and H. Raffy, Phys. Rev. Lett. **88**, 097005 (2002).
- [41] H.J.A. Molegraaf, C. Presura, D. van der Marel, P.H. Kes, and M. Li, Science **295**, 2239 (2002).
- [42] P.B. Allen, Phys. Rev. B **3**, 305 (1971).
- [43] A. Kaminski, J. Mesot, H. Fretwell, J. C. Campuzano, M. R. Norman, M. Randeria, H. Ding, T. Sato, T. Takahashi, T. Mochiku, K. Kadowaki, and H. Hoechst Phys. Rev. Lett. **84**, 1788 (2000).
- [44] A.J. Millis and H.D. Drew, Phys. Rev. B **67**, 214517 (2003).
- [45] J.P. Carbotte, E. Schachinger, and J. Hwang Phys. Rev. B **71**, 054506 (2005).
- [46] J. Hwang, T. Timusk, A.V. Puchkov, N. L. Wang, G.D. Gu, C.C. Homes, J.J. Tu, and H. Eisaki, Phys. Rev. B **69**, 094520 (2004).
- [47] C. Baraduc, A. El Azrak, and N. Bontemps, J. Supercond. **9**, 3 (1996).
- [48] A.. Abanov, A.V. Chubukov, and J. Schmalian, Phys. Rev. B **63**, 180510(R) (2001).
- [49] J.J. Tu, C.C. Homes, G.D. Gu, D.N. Basov, and M. Strongin, Phys. Rev. B **66**, 144514 (2002).
- [50] M. Vershinin, S. Misra, S. Ono, Y. Abe, Y. Ando, and A. Yazdani, Science **303**, 1995 (2004).
- [51] K. McElroy, D.-H. Lee, J.E. Hoffman, K.M. Lang, E.W. Hudson, H. Eisaki, S. Uchida, J. Lee, and J.C. Davis, cond-mat/040405.
- [52] Yoichi Ando, Seiki Komiya, Kouji Segawa, S. Ono, and Y. Kurita, Phys. Rev. Lett. **93**, 267001 (2004).
- [53] S. Uchida, T. Ido, H. Takagi, T. Arima, Y. Tokura, and S. Tajima, Phys. Rev. B **43**, 7942 (1991).
- [54] S.L. Herr, K. Kamaras, C.D. Porter, M.G. Doss, D.B. Tanner, D.A. Bonn, J.E. Greedan, C.V. Stager, and T. Timusk, Phys. Rev. B **36**, 733 (1987).
- [55] A.V. Puchkov, T. Timusk, M.A. Karlow, S.L. Cooper, P.D. Han, and D.A. Payne, Phys. Rev. B **54**, 6686 (1996).
- [56] M. Sutherland, S.Y. Li, D.G. Hawthorn, R.W. Hill, F. Ronning, M.A. Tanatar, J. Paglione, H. Zhang, L. Taillefer, J. DeBenedictis, Ruixing Liang, D.A. Bonn, and W.N. Hardy, cond-mat/0501247.
- [57] P.B. Littlewood and C.M. Varma, J. Appl. Phys. **69**, 4979 (1991).
- [58] P. Prelovsek, T. Tohyama, and S. Maekawa, Phys. Rev. B **64**, 052512 (2001).
- [59] P. Monthoux and D. Pines, Phys. Rev. B **47**, 6069 (1993).
- [60] J.P. Carbotte, Rev. Mod. Phys. **62**, 1027 (1990).
- [61] B. Mitrovic and M.A. Fiorucci, Phys. Rev. B **31**, 2694 (1985).
- [62] S.V. Shulga, O.V. Dolgov, and E.G. Maksimov, Physica C **178**, 266 (1991).
- [63] S.G. Sharapov and J.P. Carbotte, in preparation.
- [64] M. Kugler, Ø. Fischer, Ch. Renner, S. Ono, and Yoichi Ando, Phys. Rev. Lett. **86**, 4911 (2001).
- [65] C.C. Homes, T. Timusk, R. Liang, D.A. Bonn, and W.N. Hardy, Phys. Rev. Lett. **71**, 1645 (1993).
- [66] C. Stock, W.J.L. Buyers, R.A. Cowley, P.S. Clegg, R. Coldea, C.D. Frost, R. Liang, D. Peets, D. Bonn, W.N. Hardy, and R.J. Birgeneau, Phys. Rev. B **71**, 024522 (2005).
- [67] M. Gurvitch and A.T. Fiory, Phys. Rev. Lett. **59**, 1337 (1987).
- [68] T. Startseva, T. Timusk, A. V. Puchkov, D. N. Basov, H. A. Mook, M. Okuya, T. Kimura, and K. Kishio, Phys. Rev. B **59**, 7184, (1999).
- [69] T. Timusk and C.C. Homes, Solid State Comm. **126**, 63 (2003).